

High-pressure lattice-dynamics of NdVO₄

V. Panchal¹, D. Errandonea^{2,†}, F.J. Manjón³, A. Muñoz⁴, P. Rodríguez-Hernández⁴, S.N.

Achary⁵, and A.K. Tyagi⁵

¹ Royal College of Arts, Science and Commerce, Mira Road, Mumbai 401 107, India

² Departamento de Física Aplicada-ICMUV, MALTA Consolider Team, Universidad de Valencia, Edificio de Investigación, C/Dr. Moliner 50, 46100 Burjassot (Valencia), Spain

³ Instituto de Diseño para la Fabricación y Producción Automatizada, MALTA Consolider Team, Universidad Politécnica de Valencia, Camino de Vera s/n, 46022 Valencia, Spain

⁴ Departamento de Física Fundamental II, Instituto de Materiales y Nanotecnología, MALTA Consolider Team, Universidad de La Laguna, La Laguna 38205, Tenerife, Spain

⁵ Chemistry Division, Bhabha Atomic Research Centre, Trombay, Mumbai 400085, India

Abstract: High-pressure Raman-scattering measurements and *ab initio* calculations on NdVO₄ have been carried out up to 30 GPa. Our combined experimental and theoretical study confirms that beyond 5.9 GPa NdVO₄ undergoes an irreversible zircon to monazite transition. The coexistence of zircon and monazite phases is experimentally observed up to ~ 8 GPa (which agrees with the theoretical transition pressure), stabilizing the monazite phase as a single phase around 10 GPa. Calculations additionally predict the existence of a second high-pressure phase transition at 12.4 GPa. This reversible phase transition has been experimentally observed beyond 18.1 GPa and remains stable up to 30 GPa. The post-monazite phase is predicted to have a monoclinic structure isomorphic to the BaWO₄-II type structure. The calculated structure for the three polymorphs of NdVO₄ is reported and the pressure dependence of their Raman modes is discussed.

Keywords: Raman spectroscopy, Ab initio calculations, High pressure, Phase transitions

†Corresponding author; email: daniel.errandonea@uv.es

1. Introduction

The study of zircon-structured orthovanadates is important in the fields of geology and materials science. They are refractory materials, can withstand high pressures and temperatures, and generally show low thermal expansion, being useful for the ceramic industry [1]. In addition, orthovanadates found applications in thermophosphors, scintillators, photocatalysts, cathodoluminescent materials, and in lithium ion batteries [2, 3]. These materials are also used as laser-host materials when doped with trivalent impurities due to their high optical conversion efficiency, high birefringence and good thermal conductivity [4]. Recently, they have been used for the development of dual-wavelength lasers [5]. Furthermore, they can be also used to immobilize nuclear waste [6].

Rare-earth AVO_4 orthovanadates ($A = \text{Sc, Y, La - Lu}$) mostly crystallize in the tetragonal zircon-type structure (space group $I4_1/amd$) [7], although it has been found that a few orthovanadates (e.g. LaVO_4) crystallize in the monazite structure (space group $P2_1/n$), depending on the synthesis conditions and cationic size [8]. Another structure which is closely related to zircon and monazite structures is the scheelite (space group $I4_1/a$) structure. All these three structures have in common a sequence of chains of alternating polyhedral units and planes of closed packed A cations. In particular, NdVO_4 crystallizes in the tetragonal zircon structure and can be viewed as alternating edge-sharing NdO_8 dodecahedra and VO_4 tetrahedra forming chains parallel to the c -axis.

Recent investigations on orthovanadates and related ternary oxides implied a strong correlation of r_A/r_O and r_V/r_O cation-anion radius ratio on high-pressure (HP) structural phase transitions [9]. In general, orthovanadate compounds show zircon-to-scheelite [10 – 16] or zircon-to-monazite [17 -19] structural phase transitions. Some works also report post-scheelite

and post-monazite transitions [20, 21]. In addition, the compressibility and HP Raman scattering (RS) of orthovanadates have been recently explored [22 – 26]. In spite of the attention devoted to the HP study of AVO_4 orthovanadates, $NdVO_4$ is one of the less studied members of this family. Earlier HP optical-absorption measurements on $NdVO_4$ found a sharp drop in energy band-gap (E_g) from 3.72 to 3.30 eV at ~ 6 GPa. At 11.4 GPa another discontinuity in E_g was detected, indicating a second phase transition around this pressure [27]. The first drop was attributed to a zircon to monazite transition around 6.5 GPa in recent HP x-ray diffraction (XRD) measurements [18]; however, the second pressure-induced phase transition was not verified in that HP-XRD study up to 12 GPa. Here we report a combined experimental and theoretical study of HP-RS measurements and *ab initio* calculations to improve the understanding the nature of phase transitions in $NdVO_4$.

2. Experimental details

$NdVO_4$ was prepared by solid-state reaction of appropriate amounts of pre-dried Nd_2O_3 (Indian Rare Earth Ltd. 99%) and V_2O_5 (Alfa-Aesar 99%). Homogeneous mixtures of the reactants were pelletized and heated at 800 °C for 24 h and then cooled to ambient temperature. Further, the pellets were reground and heated again at 1100 °C for 24 h. X-ray diffraction measurements at ambient conditions using $Cu K\alpha$ radiation ($\lambda = 1.5418 \text{ \AA}$) confirmed a single phase with the zircon structure and $a = 7.334(1) \text{ \AA}$ and $c = 6.436(1) \text{ \AA}$, which are in very good agreement with the literature [28]. For HP-RS measurements, we used a cylindrical piece of $NdVO_4$ (40 μm in diameter and 10 μm thick). This sample and a 2- μm diameter ruby ball were loaded in a diamond-anvil cell inside a pre-indented Inconel gasket with a thickness of 40 μm and a 200- μm diameter hole. A 16:3:1 methanol-ethanol-water mixture was used as pressure-transmitting medium [29, 30]. The pressure was determined by monitoring the shift in ruby

fluorescence lines [31]. Special caution was taken to avoid sample bridging between diamonds [32]. HP Raman measurements were performed in the backscattering geometry using 632.8 nm HeNe laser with a power of 10 mW and a Horiba Jobin Yvon LabRAM high-resolution UV microspectrometer in combination with a thermoelectric-cooled multichannel CCD detector with spectral resolution below 2 cm^{-1} .

3. Theoretical method and computational details

Ab initio calculations have been performed within the density-functional theory (DFT) framework as implemented in the Vienna *ab initio* simulation package (VASP) [33]. The set of plane waves employed extended up to a kinetic energy cutoff of 520 eV. Such a large cutoff was required to achieve highly converged results within the projector-augmented-wave (PAW) scheme [34]. The exchange–correlation energy was taken in the generalized-gradient approximation (GGA) with the Perdew–Burke–Ernzerhof (PBE) prescription [35]. We used dense special point grids appropriate to each structure considered to sample the Brillouin zone (BZ), thus ensuring a high convergence of 1–2 meV per formula unit in the total energy as well as an accurate calculation of the forces on the atoms. At selected volumes, the structures were fully relaxed to their optimized configurations through the calculation of the forces on atoms and the stress tensor [36]. In the optimized configuration, the forces were smaller than $0.005 \text{ eV}/\text{\AA}$, and the deviation of the stress tensor from a diagonal hydrostatic form was less than 0.1 GPa. Lattice-dynamic calculations of the phonon modes were performed at the zone center (Γ point) of the BZ. We used the small-displacement method which has been shown to properly work to study phonons under compression [37-39]. These calculations also provide information about the symmetry of the modes and their polarization vectors, and allowed us to identify the irreducible representations and the character of the phonon modes at the Γ point.

4. Results

A. Zircon structured NdVO₄

As regards the structural properties of zircon-type NdVO₄, our *ab initio* calculations find that the tetragonal zircon is the most stable phase of NdVO₄ in agreement with previous XRD experiments [18]. This is shown in Fig. 1 where we represent the enthalpy versus pressure for different phases of interest. According with our calculations, at zero pressure and zero temperature, the lattice parameters of the zircon structure of NdVO₄ are: $a = 7.4311 \text{ \AA}$ and $c = 6.4739 \text{ \AA}$. For the oxygen position, the only one in general position by symmetry, we got (0, 0.42964, 0.20493). These calculated lattice and atomic parameters agree well with those obtained for the zircon structure of NdVO₄ from a full-profile Rietveld structure analysis of neutron powder-diffraction data [28]. As expected, our calculations overestimate the unit-cell parameters, but only by 1%. We have also obtained the pressure dependence of the unit-cell volume in the pressure range of stability of the zircon structure. By fitting this dependence with a third-order Birch-Murnaghan equation of state (EOS) [40], we determined the ambient pressure volume, $V_0 = 357.50 \text{ \AA}^3$, bulk modulus, $B_0 = 124.2 \text{ GPa}$, and its pressure derivative, $B_0' = 3.66$. While B_0' and V_0 agrees well with experiments, within the overestimation of the volume expected in DFT calculations, the calculated B_0 is 10% smaller than the experimental value [18]. Nevertheless, the calculated B_0 and B_0' lie within the 3σ confidence-level ellipse [40] determined from experiments [18]. Therefore, we can conclude that *ab initio* calculations provide a good description of the compression of the zircon structure.

As regards the vibrational properties of zircon-type NdVO₄, group theory predicts 12 Raman-active modes at the center of the BZ with symmetries $\Gamma = 2A_{1g} + 4B_{1g} + B_{2g} + 5E_g$ [41].

These modes can be further classified into internal (ν_1 - ν_4) and external (translational, T, and rotational, R) modes of VO_4 units as follows,

$$\Gamma = A_{1g}(\nu_1, \nu_2) + B_{1g}(2T, \nu_3, \nu_4) + B_{2g}(\nu_2) + E_g(2T, R, \nu_3, \nu_4).$$

Regarding the Raman spectra measured under compression, HP-RS spectra of zircon-type NdVO_4 at selected pressures are shown in Fig. 2(a). Eleven Raman-active modes are clearly discernable at ambient conditions out of the twelve predicted ones for zircon-type NdVO_4 so they can be clearly assigned to the zircon structure up to 4.9 GPa. In fact, we have followed under compression the eleven Raman-active modes up to this pressure. The only change observed is the gradual shift of the phonon frequencies as pressure increase, a typical consequence of the change of interatomic distances.

The pressure dependence of Raman-active mode frequencies in the zircon phase is plotted in Fig. 2(b) with solid circles (experiments) and lines (calculations). Most Raman modes harden under compression, but there are two modes that have a distinctive behavior. These are the external $T(E_g)$ mode at 113 cm^{-1} , which shows very small pressure coefficient and the internal $\nu_2(B_{2g})$ mode at 260 cm^{-1} , which shows a negative pressure coefficient. In addition, we found that there are two pairs of modes which gradually merge under compression due to their different pressure dependence. These are the modes at 243.1 and 260.9 cm^{-1} and at 373.4 and 381.9 cm^{-1} at ambient pressure. The symmetry assignment for the experimental Raman-active modes along with their experimental and calculated frequencies and pressure coefficients are summarized in Table 1. It must be noted that the pressure coefficients of all the Raman modes are comparable with other orthovanadates [10, 19, 22, 24, 26]. In order to complete the description of the HP behavior of the Raman-active modes of zircon-type NdVO_4 in Table 1 we include the mode Grüneisen parameters, $\gamma = (B_0/\omega_0)(d\omega/dP)$, where $B_0 = 148 \text{ GPa}$ is the bulk modulus [18]. These

parameters are useful to estimate the pressure dependence of thermodynamic, elastic, and transport properties.

The symmetry assignment for the Raman-active modes has been performed in accordance with our lattice dynamics calculations and with previous polarized Raman studies [41, 42]. The agreement between experiments and calculations is quite good. The difference among the measured and calculated wavenumbers (ω) is smaller than 4% for all the measured modes. When comparing the pressure coefficients ($d\omega/dP$) we observe a similar agreement. In only one mode, the lowest frequency mode, the calculated pressure coefficient is considerable larger than the experimental coefficient.

Taking into account the good agreement between our experimental and theoretical frequencies and pressure coefficients it was rather easy to make a tentative assignment of the symmetry of the Raman-active modes experimentally observed. In this sense, the highest frequency Raman mode, the most intense mode, is the symmetric-stretching internal mode $\nu_1(A_{1g})$, observed at 871 cm^{-1} at ambient pressure. There are also two other high-frequency modes, these are the two asymmetric-stretching modes $\nu_3(E_g)$ and $\nu_3(B_{1g})$ recorded at 808 and 794 cm^{-1} , respectively. The rest of the modes are below 475 cm^{-1} and correspond to either bending modes of the VO_4 unit or to external (translational and rotational) modes. Regarding the bending modes of the VO_4 unit, we have observed: $\nu_4(B_{1g})$ at 472 cm^{-1} , $\nu_2(A_{1g})$ at 381 cm^{-1} , $\nu_4(E_g)$ at 373 cm^{-1} , and $\nu_2(B_{2g})$ at 260 cm^{-1} respectively. The translational modes correspond to the four modes found at the lowest frequencies. The only Raman mode absent is the rotational mode $R(E_g)$, which is theoretically predicted at 224.6 cm^{-1} and has the largest pressure coefficient of all Raman-active modes.

As regards the assignment of the symmetry of the absent Raman-active mode in rare-earth zircon-type vanadates, there is an ongoing discussion in the literature regarding why in most cases only 11 of the 12 Raman-active modes are observed and which is the non-observed mode. In most cases, the rotational mode $R(E_g)$ or the bending $\nu_4(E_g)$ mode is the one usually assumed to be not observed in these compounds [41, 42]. In this respect, HP-RS measurements can be very helpful in order to clarify which one is the absent mode. The present HP-RS measurements in $NdVO_4$ have allowed us to find that the absent mode is the bending $\nu_4(E_g)$ mode, unlike previously assumed [41, 42]. Similarly, previous HP-RS measurements in $ScVO_4$ and $TbVO_4$ helped us to find that the absent mode was also the bending $\nu_4(E_g)$ mode [10, 26]. However, in $CeVO_4$ it seems that the lost mode is the bending mode $\nu_2(A_{1g})$ mode, which has a much larger pressure coefficient than the bending $\nu_4(E_g)$ mode [43]. In the case of $YbVO_4$, $PrVO_4$, and $SmVO_4$, HP-RS measurements were not correlated to *ab initio* calculations [19, 23]; however, taking into account the large pressure coefficient typical of the rotational $R(E_g)$ mode, and the fact that the bending $\nu_4(E_g)$ mode has a frequency near 350 cm^{-1} ; i.e., close to that of the bending $\nu_2(A_{1g})$ mode, we can safely conclude that the lost mode in these vanadates is also the bending $\nu_4(E_g)$ mode in both compounds. Moreover, since our calculations on zircon-type rare-earth orthovanadates $ScVO_4$ [10], $TbVO_4$ [26], $CeVO_4$ [43], and $NdVO_4$ (this work) have shown that both modes, one $T(E_g)$ and the $\nu_2(B_{2g})$ mode, have always a negative pressure coefficient, we can conclude that the Raman-active mode observed at $261\text{-}262\text{ cm}^{-1}$ with negative pressure coefficient in $YbVO_4$, $PrVO_4$ and $SmVO_4$ correspond to the $\nu_2(B_{2g})$ mode and not to the $T(B_{1g})$ as was previously assigned [19, 23].

B. Monazite structured NdVO₄

In the structural calculations we found the occurrence of a transition from the zircon to a monazite structure at 8.5 GPa. This is consistent with the irreversible phase transition determined from XRD measurements at 6.5 GPa [18] and with the changes observed in the optical properties of NdVO₄ at 6 GPa [27]. The XRD patterns measured for the HP phase have been assigned to a monazite-type structure [18], however a full structural refinement of the HP phase was not possible. Here we provide the complete structural description of the monazite structure (space group P2₁/n, Z = 4), which is given in Table 2. The monazite phase is closely related to the zircon structure. Monazite can be viewed as being composed by alternating edge-sharing NdO₉ polyhedra and VO₄ tetrahedra [44]. The calculated unit-cell parameters of monazite-type NdVO₄ ($a = 6.80545 \text{ \AA}$, $b = 7.05855 \text{ \AA}$, $c = 6.54038$, and $\beta = 104.62^\circ$ at 9.8 GPa) are similar to those determined from XRD ($a = 6.83 \text{ \AA}$, $b = 6.99 \text{ \AA}$, $c = 6.51 \text{ \AA}$, and $\beta = 104.7^\circ$ at 10.8 GPa).

The zircon-monazite phase transition involves a 9% volume collapse. From our calculations we also determined the pressure dependence of the unit-cell volume, which is described by a third-order Birch-Murnaghan EOS [40] with $V_0 = 316.62 \text{ \AA}^3$, $B_0 = 138.8 \text{ GPa}$, and $B_0' = 3.79$. The values of B_0 (12% larger than in the zircon phase) and B_0' (4% larger than in the zircon phase) suggests that the monazite phase is less compressible than the zircon phase. A feature that has been observed in other vanadates [20, 21] and it is related to the increase of the packing efficiency in the monazite structure with respect to the zircon structure.

As regards the vibrational properties of monazite-type NdVO₄, group theoretical calculations predict 36 vibrational Raman modes at the BZ centre with following symmetries $\Gamma = 18A_g + 18B_g$ [45]. These modes can be further classified into internal (ν_1 - ν_4) and external (translational, T, and rotational, R) modes of VO₄ units as follows,

$$\Gamma = A_g(6T, 3R, \nu_1, 2\nu_2, 3\nu_3, 3\nu_4) + B_g(6T, 3R, \nu_1, 2\nu_2, 3\nu_3, 3\nu_4).$$

Fig. 3(a) shows the Raman spectra of NdVO₄ in the monazite phase at a few representative pressures. It can be seen that at 5.9 GPa we have observed noticeable changes in the Raman spectrum with emergence of new Raman bands, accompanied by the broadening of many Raman modes. These changes in the Raman spectra are indicative of a structural phase transition towards the lower-symmetry monoclinic monazite phase. This is in quite agreement with our calculations and previous experiments [18, 25]. The monazite phase is predicted to be observed up to 12.4 GPa according to our calculations and was observed up to 18.1 GPa in our experiments [18]. The difference in the transition pressure can be related to the presence of a kinetic energy barrier between the monazite and post-monazite structures.

We have observed twenty-one Raman modes at 6.3 GPa out of thirty-six Raman modes predicted for the monazite phase of NdVO₄. Similarly, in Raman scattering measurements of CeVO₄, twenty-seven Raman modes were detected after the zircon-to-monazite phase transition [41]. In addition, to the Raman modes of the monazite phase, the most intense Raman mode of the zircon phase (the highest frequency mode) is observed up to ~ 8 GPa, suggesting a phase coexistence during a 3 GPa range.

Fig. 3(b) shows the experimental (symbols) and theoretical (lines) pressure dependence of the Raman-active modes of monazite-type NdVO₄. The mode assignment of the experimentally-observed Raman modes in monazite NdVO₄ was carried out by comparing the experimental and calculated values of frequencies and pressure coefficients and is shown in Table 3. In the table we also provide the mode Grüneisen parameters calculated assuming $B_0 = 138.8$ GPa. The calculated Raman frequencies and their pressure coefficients are in good agreement with our experimental ones. The Raman modes can be divided in two groups of modes, one for $\omega > 750$

cm^{-1} and the other with $\omega < 460 \text{ cm}^{-1}$, resembling the Raman spectra of monazite-type selenates and chromates, which have been recently studied in an exhaustive way [46]. The eight high-frequency modes correspond to the internal stretching modes of the VO_4 tetrahedron. This number is double the number of internal modes of the zircon phase (taking into account the double degeneration of the $\nu_3(\text{E}_g)$ mode in the zircon phase) because of the reduction of the crystal-symmetry of monazite, which among other things transform the regular VO_4 polyhedron of the zircon phase into an irregular tetrahedron with four different V-O distances in the monazite phase, and the doubling of the primitive unit-cell. The rest of the modes correspond to internal bending modes and external modes. As expected, the internal stretching modes are the most intense modes in our experiments.

Regarding the pressure dependence of the Raman-active modes we found that under compression most modes harden (See Fig. 3(b) and Table 3); however, we have observed a small softening of two Raman modes of A_g symmetry at 95 cm^{-1} and 139 cm^{-1} . Calculations also predict the presence of a low-frequency B_g mode with a negative pressure coefficient. Similarly, three soft modes were theoretically predicted for monazite-type CeVO_4 [43]. It must be stressed that the wavenumbers of these three modes never reach zero in the pressure range of stability of the monazite phase. This result indicates that they are not classical soft-modes, as those observed in a second-order displacive transition [47]. A similar weak softening of two or three modes has been previously found in monazite-type CeVO_4 , PbCrO_4 and LaVO_4 [41, 48, 49]. The presence of such modes has been correlated with a weakening of the restoring force against the corresponding deformation associated to the soft phonon mode, marking probably the existence of a collective instability that tends to make the crystal structure unstable [50]. This fact is consistent with the finding of a phase transition to a post-monazite phase as we found.

C. Post-monazite phase

A strong decrease of the bandgap near 11.4 GPa was found in NdVO₄ by optical-absorption experiments [27]. This change correlates with the fact that RS spectra measured from 19 GPa to 30.8 GPa (see Fig. 4) are quite different from those measured up to 18.1 GPa. These experimental results suggest the existence of a second phase transition in NdVO₄. The existence of this second phase transition, above 12.4 GPa, is supported by our calculations, as can be seen in Fig. 1. Therefore, we think there is enough evidence to support the existence of a post-monazite phase in NdVO₄. In a previous work, a tentative phase transition to the scheelite phase was proposed [27]; however, in this work we have carried out calculations for a larger number of candidate structures on the light of the Bastide's diagram [8]. Our improved calculations suggest the possibility that the post-monazite phase in NdVO₄ is of BaWO₄-II-type. A similar structure has been proposed as a HP structure in related oxides BaWO₄, PbWO₄, and SrMO₄ [51 - 53]. The Raman spectra of such phases [53 - 56] have qualitative similitudes with the Raman spectrum of the post-monazite phase of NdVO₄.

Details on the crystal structure of the BaWO₄-II structure of NdVO₄ are given in Table 4. This structure is monoclinic (space group P2₁/n, Z = 8) and can be described with the same space group than monazite, however it has 8 formula units in the unit cell instead of 4. The phase transition involves an increase of the coordination number for both V and Nd and there is a volume collapse associated to it. Its EOS is described by the following parameters: V₀ = 596.35 Å³, B₀ = 146.8 GPa, and B₀' = 3.42. This indicates that, the post-monazite phases have slightly smaller volume compressibility than the monazite phase.

As regards the vibrational properties of the BaWO₄-II-type NdVO₄, group theory predicts 72 Raman-active modes (36A_g and 36B_g). The number of Raman modes is double in the BaWO₄-II

phase than in monazite, despite they share the same space group, because of the double number of formula units in the primitive cell of this phase than in the monazite structure. The calculated wavenumber and pressure dependence of the different modes is given in Table 5. In contrast with the other two phases, in the BaWO₄-II-type phase all pressure coefficients are positive. Another distinctive feature of the post-monazite phase is that phonons are continuously distributed from 80 to 950 cm⁻¹. In contrast, the zircon and monazite phases have a large phonon gap between the internal stretching mode and the rest of the modes as we commented above. It is possible that, due to this large number of modes and because many of them are very close in frequency, a considerable broadening in the Raman spectrum on the post-monazite phase was observed. This broadening precludes us of making an accurate frequency determination of the different modes of the post-monazite phase. Therefore, from the experiments we can only state that there exist a post-monazite phase and that it has a Raman spectrum similar to that expected for a BaWO₄-II structure. The calculated phonon frequencies, pressure coefficients, and the mode Grüneisen parameters (calculated using $B_0 = 146.8$ GPa) are summarized in Table 5.

It is important to note that despite the observation of a broad band at high frequencies, makes difficult an individual analysis of the different internal modes which are very close in frequency, a general drop in the average frequency of the broad band of intense high-frequency modes on the transition from monazite-to-BaWO₄-II can be observed. This drop in frequency is consistent with the increase of the V coordination in the BaWO₄-II-type phase with respect to the monazite-type phase. Therefore, on the light of the exposed results we are confident that the second HP phase of NdVO₄ is the BaWO₄-II structure. Furthermore, the monazite-BaWO₄-II phase transition is consistent with Bastide's diagram [8] because in some materials the monazite-scheelite phase transition can be skipped and undergo a phase transition directly to a post-

scheelite phase, as evidenced in PbWO_4 and BaWO_4 [50 - 53]. Additionally, monazite LaVO_4 has been recently reported to undergo a monazite- BaWO_4 -II transition [48], which suggests that the BaWO_4 -II structure might be a common post-monazite phase in AVO_4 vanadates if the trivalent cation has a large ionic radius (La, Ce, Nd, and Pr).

5. Conclusions

Our Raman experiments and *ab initio* calculations on NdVO_4 up to 30.8 GPa provides evidence supporting that the low-pressure zircon phase undergo an irreversible zircon-to-monazite transition at 5.9 GPa. The symmetries of the Raman modes in the zircon and monazite phases of NdVO_4 have been assigned in accordance with our lattice dynamics calculations. The pressure dependence of the different modes is discussed. In particular, both zircon and monazite phases have modes that undergo a weak softening under compression. Beyond 18.1 GPa NdVO_4 undergoes a second phase transition. Our calculations predict a monazite-to- BaWO_4 -II phase transition. Details on the calculated crystal structure of the three polymorphs of NdVO_4 are reported together with their room temperature equation of states. The calculated Raman modes for the BaWO_4 -II phase are also reported. The RS spectra of NdVO_4 are reasonably consistent with the BaWO_4 -II phase. Further HP-XRD measurements, at least up to 25 GPa, are needed to fully check the BaWO_4 -II nature of the second HP phase of NdVO_4 .

Acknowledgments

The authors thank the financial support provided by the Spanish government MINECO under Grants No: MAT2013-46649-C4-1/2/3 and MAT2015-71070-REDC.

References

[1] S. J. Patwe, S. N. Achary, A. K. Tyagi, Lattice thermal expansion of zircon-type LuPO_4 and LuVO_4 : A comparative study, *American Mineral.* 94 (2009) 98–104.

- [2] S. P. Shafi, M. W. Kotyk, L. M. D. Cranswick, V. K. Michaelis, S. Kroeker, and M. Bieringer, In Situ Powder X-ray Diffraction, Synthesis, and Magnetic Properties of the Defect Zircon Structure ScVO_{4-x} , *Inor. Chem.* 48 (2009) 10553-10559.
- [3] J. Xu, C. Hu, G. Liu, H. Liu, G. Du, Y. Zhang, Synthesis and visible-light photocatalytic activity of NdVO_4 nanowires, *J. Alloys Compd.* 509 (2011) 7968–7972.
- [4] D. Zhong, B. Teng, W. Kong, J. Li, S. Zhang, Y. Li, L. Cao, L. Yang, L. He, W. Huang, Growth, thermal and laser properties of $\text{Yb:Y}_x\text{Lu}_{1-x}\text{VO}_4$ mixed crystal, *Mater. Chem. Phys.* 160 (2015) 155–160.
- [5] Z. Wu, Z. Wang, F. Zhang, Y. Liu, J. Lu, X. Xu, Optical frequency fork based on stimulated Raman scattering, *J. Alloys Compd.* 682 (2016) 537–542.
- [6] Y. Ding, X. Lu, H. Dan, X. Shu, S. Zhang, T. Duan, Phase evolution and chemical durability of Nd-doped zircon ceramics designed to immobilize trivalent actinides, *Ceram. Intern.* 41(2015) 10044-10050.
- [7] A. B. Garg, D. Errandonea, P. Rodriguez-Hernandez, S. Lopez-Moreno, A. Muñoz, C. Popescu, High-pressure structural behaviour of HoVO_4 : combined XRD experiments and *ab initio* calculations, *J. Phys. Condens. Matter* 26 (2014) 265402.
- [8] X. R. Cheng, D. J. Guo, S. Q. Feng, K. Yang, Y. Q. Wang, Y. F. Ren, Y. Song, Structure and stability of monazite- and zircon-type LaVO_4 under hydrostatic pressure, *Optic. Mater.* 49 (2015) 32–38.
- [9] D. Errandonea, F. J. Manjón, Pressure effects on the structural and electronic properties of ABX_4 scintillating crystals, *Prog. Mater. Sci.* 53 (2008) 711-773.

- [10] V. Panchal, F. J. Manjón, D. Errandonea, P. Rodríguez Hernández, J. López-Solano, A. Muñoz, S. N. Achary, A. K. Tyagi, High-pressure study of ScVO_4 by Raman scattering and *ab initio* calculation, *Phys. Rev. B* 83 (2011) 064111.
- [11] D. Errandonea, R. Lacomba-Perales, J. Ruiz-Fuertes, A. Segura, S. N. Achary, A. K. Tyagi, High-pressure structural investigation of several zircon-type orthovanadates, *Phys. Rev. B* 79 (2009) 184104.
- [12] F. J. Manjón, P. Rodríguez-Hernández, A. Muñoz, A. H. Romero, D. Errandonea, Lattice dynamics of YVO_4 at high pressures, *Phys. Rev. B* 81 (2010) 075202.
- [13] R. Rao, A. B. Garg, T. Sakuntala, S. N. Achary, A. K. Tyagi, High pressure Raman scattering study on the phase stability of LuVO_4 , *J. Solid. State Chem.* 182 (2009) 1879-1883.
- [14] C. Popescu, A. B. Garg, D. Errandonea, J. A. Sans, P. Rodriguez-Hernandez, S. Radescu, A. Muñoz, S. N. Achary, A. K. Tyagi, Pressure-induced phase transformation in zircon-type orthovanadate SmVO_4 from experiment and theory, *J. Phys. Condens. Matter* 28 (2016) 035402.
- [15] A. B. Garg, D. Errandonea, High-pressure powder x-ray diffraction study of EuVO_4 , *J. Solid. State Chem.* 226 (2015) 147–153.
- [16] Z. Huang, L. Zhang, W. Pan, Physical properties of zircon and scheelite lutetium orthovanadate: Experiment and first-principles calculation, *J. Solid. State Chem.* 205 (2013) 97–103.
- [17] H. Yuan, K. Wang, C. Wang, B. Zhou, K. Yang, J. Liu, B. Zou, Pressure-Induced Phase Transformations of Zircon-Type LaVO_4 Nanorods, *J. Phys. Chem. C* 119 (2015) 8364–8372.
- [18] D. Errandonea, C. Popescu, S. N. Achary, A. K. Tyagi, M. Bettinelli, In situ high-pressure synchrotron X-ray diffraction study of the structural stability in NdVO_4 and LaVO_4 , *Mat. Res. Bull.* 50 (2014) 279-284.

- [19] D. Errandonea, S.N. Achary, J. Pellicer-Porres, A.K. Tyagi, Pressure-Induced Transformations in PrVO_4 and SmVO_4 and Isolation of High-Pressure Metastable Phases, *Inorg. Chem.* 52 (2013) 5464-5469.
- [20] D. Errandonea, R.S. Kumar, S.N. Achary, A.K. Tyagi, *In situ* high-pressure synchrotron x-ray diffraction study of CeVO_4 and TbVO_4 up to 50 GPa, *Phys. Rev. B* 84 (2011) 224121.
- [21] A. B. Garg, K. V. Shanavas, B. N. Wani, S. M. Sharma, Phase transition and possible metallization in CeVO_4 under pressure, *J. Solid State Chem.* 203 (2013) 273.
- [22] W. Paszkowicz, J. Lopez-Solano, P. Piszora, B. Bojanowski, A. Mujica, A. Muñoz, Y. Cerenius, S. Carlson, H. Dabkowska, Equation of state and electronic properties of EuVO_4 : A high-pressure experimental and computational study, *J. Alloys Compd.* 648 (2015) 1005-1016.
- [23] A. B. Garg, R. Rao, T. Sakuntala, B. N. Wani, V. Vijayakumar, Phase stability of YbVO_4 under pressure: *In situ* x-ray and Raman spectroscopic investigations, *J. Appl. Phys.* 106 (2009) 063513.
- [24] Z. Huang, L. Zhang, W. Pan, Synthesis, Lattice Dynamics, and Mechanical Properties of a High-Pressure Scheelite Phase of RVO_4 , *Inorg Chem.* 51 (2012) 11235–11237.
- [25] V. Panchal, D. Errandonea, F. J. Manjon, A. Muñoz, P. Rodriguez-Hernandez, M. Bettinelli, S. N. Achary, A. K. Tyagi, High pressure phase transitions in NdVO_4 , *AIP Conference Proceedings* 1665 (2015) 030006.
- [26] D. Errandonea, F. J. Manjon, A. Muñoz, P. Rodriguez-Hernandez, V. Panchal, S. N. Achary, A. K. Tyagi, High-pressure polymorphs of TbVO_4 : A Raman and *ab initio* study, *J. Alloys Compd.* 577 (2013) 327–335.

- [27] V. Panchal, D. Errandonea, A. Segura, P. Rodríguez-Hernandez, A. Muñoz, S. Lopez-Moreno, and M. Bettinelli, The electronic structure of zircon-type orthovanadates: Effects of high-pressure and cation substitution, *J. App. Phys.* 110 (2011) 043723.
- [28] B. C. Chakoumakos, M. M. Abraham, L. A. Boatner, Crystal Structure Refinements of Zircon-Type MVO_4 ($M = Sc, Y, Ce, Pr, Nd, Tb, Ho, Er, Tm, Yb, Lu$), *J. Solid State Chem.* 109 (1994) 197–202.
- [29] S. Klotz, L. Paumier, G. Le Marchand, and P. Munsch, Hydrostatic limits of 11 pressure transmitting media, *J. Phys. D: Appl. Phys.* 42 (2009) 075413.
- [30] D. Errandonea, Y. Meng, M. Somayazulu, and D. Häusermann, Pressure-induced $\alpha \rightarrow \omega$ transition in titanium metal: a systematic study of the effects of uniaxial stress, *Physica B* 355 (2005) 116-125.
- [31] H. K. Mao, J. Xu, and P. M. Bell, Calibration of the Ruby Pressure Gauge to 800 kbar Under Quasi-Hydrostatic Conditions, *J. Geophys. Res.* 91 (1986) 4673-4676.
- [32] D. Errandonea, Exploring the properties of MTO_4 compounds using high-pressure powder x-ray diffraction, *Cryst. Res. Technol.* 50 (2015) 729-736.
- [33] G. Kresse, J. Furthmuller, Efficient iterative schemes for *ab initio* total-energy calculations using a plane-wave basis set, *Phys. Rev. B* 54 (1996) 11169.
- [34] C.J. Pickard, B. Winkler, R.K. Chen, M.C. Payne, M.H. Lee, J.S. Lin, J.A. White, V. Milman, D. Vanderbilt, Structural Properties of Lanthanide and Actinide Compounds within the Plane Wave Pseudopotential Approach, *Phys. Rev. Lett.* 85 (2000) 5122.
- [35] J.P. Perdew, K. Burke, M. Ernzerhof, Generalized Gradient Approximation Made Simple, *Phys. Rev. Lett.* 77 (1996) 3865.

- [36] A. Mujica, A. Rubio, A. Muñoz, R.J. Needs, High-pressure phases of group-IV, III–V, and II–VI compounds, *Rev. Mod. Phys.* 75 (2003) 863.
- [37] K. Parlinski, computer code PHONON. <<http://wolf.ifj.edu.pl/phonon/>>.
- [38] C. Cazorla and J. Iñiguez, Insights into the phase diagram of bismuth ferrite from quasiharmonic free-energy calculations, *Phys. Rev. B* 88 (2013) 214430.
- [39] C. Cazorla and J. Boronat, First-principles modeling of quantum nuclear effects and atomic interactions in solid He⁴ at high pressure, *Phys. Rev. B* 91(2015) 024103.
- [40] R. J. Angel, Equations of State, *Reviews in Mineral. Geochem.* 41 (2000) 35–60.
- [41] A.-D. Nguyen, K. Murdoch, N. Edelstein, L. A. Boatner, and M. M. Abraham, Polarization dependence of phonon and electronic Raman intensities in PrVO₄ and NdVO₄, *Phys. Rev. B* 56 (1997) 7974.
- [42] I. Guedes, Y. Hirano, M. Grimsditch, N. Wakabayashi, C. K. Loong, L. A. Boatner, Raman study of phonon modes in ErVO₄ single crystals, *J. Appl. Phys.* 90 (2001) 1843.
- [43] V. Panchal, S. Lopez-Moreno, D. Santamaria-Perez, D. Errandonea, F. J. Manjon, P. Rodriguez-Hernandez, A. Muñoz, S. N. Achary, A. K. Tyagi, Zircon to monazite phase transition in CeVO₄: X-ray diffraction and Raman-scattering measurements, *Phys. Rev. B* 84 (2011) 024111.
- [44] R. Lacomba-Perales, D. Errandonea, Y. Meng, M. Bettinelli, High-pressure stability and compressibility of APO₄ (A = La, Nd, Eu, Gd, Er, and Y) orthophosphates: An x-ray diffraction study using synchrotron radiation, *Phys. Rev. B* 81 (2010) 064113.
- [45] G. M. Begun, G. W. Beall, A. Boatner, W. J. Gregor, Raman spectra of the rare earth orthophosphates, *J. Raman Spectr.* 11 (1981) 273-278.

- [46] D. Errandonea, A. Muñoz, P. Rodríguez-Hernández, J. E. Proctor, F. Sapiña, M. Bettinelli, Theoretical and Experimental Study of the Crystal Structures, Lattice Vibrations, and Band Structures of Monazite-Type PbCrO_4 , PbSeO_4 , SrCrO_4 , and SrSeO_4 , *Inorg. Chem.* 54 (2015) 7524–7535.
- [47] M.T. Dove, Theory of displacive phase transitions in minerals, *Am. Mineral.* 82 (1997) 213-244.
- [48] E. Bandiello, D. Errandonea, D. Martinez-Garcia, D. Santamaria-Perez, F.J. Manjón, Effects of high-pressure on the structural, vibrational, and electronic properties of monazite-type PbCrO_4 , *Phys. Rev. B* 85 (2012) 024108.
- [49] D. Errandonea, J. Pellicer-Porres, D. Martínez-García, J. Ruiz-Fuertes, A. Friedrich, W. Morgenroth, C. Popescu, P. Rodriguez-Hernandez, A. Muñoz, M. Bettinelli, Phase Stability of Lanthanum Orthovanadate at High Pressure, *J. Phys. Chem. C* 120 (2016) 13749–13762.
- [50] D. Errandonea, J. Pellicer-Porres, M.C. Pujol, J. J. Carvajal, M. Aguiló, Room-temperature vibrational properties of potassium gadolinium double tungstate under compression up to 32 GPa, *J. Alloys Compd.* 638 (2015) 14-20.
- [51] D. Errandonea, J. Pellicer-Porres, F. J. Manjón, A. Segura, Ch. Ferrer-Roca, R. S. Kumar, O. Tschauer, J. López-Solano, P. Rodríguez-Hernández, S. Radescu, A. Mujica, A. Muñoz, G. Aquilanti, Determination of the high-pressure crystal structure of BaWO_4 and PbWO_4 , *Phys. Rev. B* 73 (2006) 224103.
- [52] O. Gomis, J. A. Sans, R. Lacomba-Perales, D. Errandonea, Y. Meng, J. C. Chervin, A. Polian, Complex high-pressure polymorphism of barium tungstate, *Phys. Rev. B* 86 (2012) 054121.

- [53] D. Errandonea, L. Gracia, R. Lacomba-Perales, A. Polian, and J. C. Chervin, Compression of scheelite-type SrMoO_4 under quasi-hydrostatic conditions: Redefining the high-pressure structural sequence, *J. Appl. Phys.* 113 (2013) 123510.
- [54] F. J. Manjón, D. Errandonea, N. Garro, J. Pellicer-Porres, P. Rodríguez-Hernández, S. Radescu, J. López-Solano, A. Mujica, A. Muñoz, Lattice dynamics study of scheelite tungstates under high pressure I. BaWO_4 , *Phys. Rev. B* 74 (2006) 144111.
- [55] F. J. Manjón, D. Errandonea, N. Garro, J. Pellicer-Porres, P. Rodríguez-Hernández, S. Radescu, J. López-Solano, A. Mujica, A. Muñoz, Lattice dynamics study of scheelite tungstates under high pressure II. PbWO_4 , *Phys. Rev. B* 74 (2006) 144112.
- [56] D. Errandonea, R. Lacomba-Perales, K.K. Mishra, A. Polian, *In-situ* high-pressure Raman scattering studies in PbWO_4 up to 48 GPa, *J. Alloys Compd.* 667 (2016) 36-43.

Table 1: *Ab initio* calculated and experimental frequencies at ambient conditions, pressure coefficients, and Grüneisen parameters in zircon-type NdVO₄.

Raman Mode Symmetry	Experiment			Theory		
	ω_0 [cm ⁻¹]	$d\omega/dP$ [cm ⁻¹ /GPa]	γ	ω_0 [cm ⁻¹]	$d\omega/dP$ [cm ⁻¹ /GPa]	γ
T(E _g)	113.0	0.26	0.34	112.1	0.86	1.14
T(B _{1g})	123.8	0.64	0.77	122.3	0.93	1.13
T(E _g)	151.1	0.44	0.43	149.7	0.27	0.27
R(E _g)	-----	-----	--	224.6	5.22	3.44
T(B _{1g})	243.1	2.66	1.62	233.9	2.95	1.87
ν_2 (B _{2g})	260.9	-1.32	-0.75	258.2	-1.59	-0.91
ν_4 (E _g)	373.4	2.10	0.83	363.9	1.61	0.65
ν_2 (A _{1g})	381.9	1.76	0.68	365.5	1.80	0.73
ν_4 (B _{1g})	472.2	2.31	0.72	453.0	2.62	0.86
ν_3 (B _{1g})	794.6	5.42	1.01	797.0	6.30	1.17
ν_3 (E _g)	808.1	4.95	0.91	801.9	5.75	1.06
ν_1 (A _{1g})	871.1	5.63	0.96	859.0	6.35	1.09

Table 2: Crystal structure of monazite-type NdVO₄ calculated at 9.8 GPa (space group P2₁/n).

The Wyckoff positions of different atoms are indicated between brackets.

<i>a</i>	6.8055 Å
<i>b</i>	7.0586 Å
<i>c</i>	6.5404 Å
β	104.62°
Nd (4e)	(0.27418, 0.15669, 0.10826)
V (4e)	(0.29786, 0.16643, 0.62062)
O ₁ (4e)	(0.23940, 0.99567, 0.42449)
O ₂ (4e)	(0.38786, 0.35221, 0.50284)
O ₃ (4e)	(0.48915, 0.11009, 0.83547)
O ₄ (4e)	(0.11121, 0.22502, 0.74158)

Table 3: *Ab initio* calculated frequencies (at 7.3 GPa) and experimental frequencies (at 6.4 GPa), pressure coefficients, and Grüneisen parameters in monazite-type NdVO₄.

Raman Mode Symmetry	Experiment			Theory		
	ω [cm ⁻¹]	$d\omega/dP$ [cm ⁻¹ /GPa]	γ	ω [cm ⁻¹]	$d\omega/dP$ [cm ⁻¹ /GPa]	γ
Bg	58.0	1.00	2.41	56.5	0.21	0.52
Ag	76.1	0.29	0.53	74.3	0.29	0.55
Bg	----	----	----	95.7	-0.55	-0.80
Ag	95.9	-0.28	-0.41	97.2	-0.27	-0.39
Ag	113.1	0.25	0.31	112.5	0.38	0.47
Bg	----	----	----	128.5	0.75	0.82
Bg	----	----	----	129.8	1.42	1.53
Ag	139.2	-0.55	-0.55	140.7	-0.37	-0.37
Ag	144.1	0.86	0.84	156.3	1.00	0.90
Bg	158.6	2.10	1.85	168.2	1.89	1.57
Ag	----	----	----	176.6	1.13	0.90
Ag	190.3	2.66	1.96	205.5	2.52	1.72
Bg	----	----	----	209.6	2.19	1.46
Bg	226.6	1.59	0.98	232.1	1.63	0.98
Bg	----	----	----	247.6	2.45	1.39
Ag	----	----	----	255.4	1.47	0.81
Bg	263.2	2.77	1.47	263.6	2.84	1.51
Ag	291.4	2.37	1.14	279.1	2.96	1.48
Bg	310.6	2.39	1.08	305.5	1.89	0.87
Ag	----	----	----	328.7	1.00	0.43
Bg	----	----	----	336.2	2.09	0.87
Ag	362.2	3.44	1.33	356.9	2.68	1.05
Ag	378.8	3.75	1.39	382.3	3.67	1.34
Ag	399.4	4.03	1.41	406.0	3.19	1.10
Bg	----	----	----	412.4	2.49	0.85
Bg	427.7	3.58	1.17	424.5	2.21	0.73
Ag	----	----	----	444.5	2.78	0.88
Bg	459.2	3.41	1.04	456.6	3.77	1.16
Ag	762.9	5.49	1.01	788.8	3.59	0.64
Bg	----	----	----	804.2	3.51	0.61
Ag	822.3	3.88	0.66	817.6	4.23	0.72
Ag	854.7	3.32	0.54	850.2	2.26	0.37
Bg	----	----	----	861.5	4.69	0.76
Ag	----	----	----	881.9	3.72	0.59
Bg	----	----	----	882.6	3.40	0.54
Bg	890.9	2.54	0.40	902.7	2.41	0.37

Table 4: Crystal structure of BaWO₄-II-type NdVO₄ calculated at 15.8 GPa (space group P2₁/n). The Wyckoff positions of different atoms are indicated between brackets.

<i>a</i>	12.3630 Å
<i>b</i>	6.4442 Å
<i>c</i>	6.8174 Å
β	96.16°
Nd ₁ (4e)	(0.89292, 0.83968, 0.11759)
Nd ₂ (4e)	(0.87508, 0.55366, 0.63608)
V ₁ (4e)	(0.87160, 0.32781, 0.17440)
V ₂ (4e)	(0.83104, 0.05367, 0.60301)
O ₁ (4e)	(0.93827, 0.53816, 0.32154)
O ₂ (4e)	(0.79256, 0.86204, 0.77774)
O ₃ (4e)	(0.90259, 0.89948, 0.46801)
O ₄ (4e)	(0.77872, 0.13698, 0.08896)
O ₅ (4e)	(0.91798, 0.19443, 0.75993)
O ₆ (4e)	(0.80881, 0.27289, 0.41770)
O ₇ (4e)	(0.98972, 0.19608, 0.14742)
O ₈ (4e)	(0.83469, 0.51500, 0.98392)

Table 5: *Ab initio* calculated frequencies, pressure coefficients, and Grüneisen parameters in BaWO₄-II-type NdVO₄ at 15.8 GPa.

Raman Mode Symmetry	ω [cm ⁻¹]	d ω /dP [cm ⁻¹ /GPa]	γ	Raman Mode Symmetry	ω [cm ⁻¹]	d ω /dP [cm ⁻¹ /GPa]	γ
Ag	82.24	1.73	3.09	Bg	362.54	2.71	1.10
Bg	82.24	1.73	3.09	Bg	376.87	3.82	1.49
Bg	90.84	0.81	1.31	Ag	415.58	6.35	2.24
Ag	100.51	0.50	0.73	Bg	386.19	0.88	0.34
Bg	110.61	1.08	1.43	Ag	398.15	0.98	0.36
Ag	106.28	0.37	0.51	Bg	414.17	3.05	1.08
Ag	140.28	2.18	2.28	Ag	415.24	0.66	0.23
Bg	134.99	0.55	0.60	Bg	415.24	0.66	0.23
Ag	150.41	3.72	3.63	Bg	431.60	1.96	0.67
Bg	146.80	2.52	2.52	Bg	431.90	2.62	0.89
Ag	146.34	0.50	0.50	Ag	454.11	3.63	1.17
Bg	168.18	2.46	2.14	Ag	445.91	3.32	1.09
Ag	163.88	1.17	1.05	Ag	459.37	3.56	1.14
Bg	189.42	2.32	1.80	Ag	477.04	1.91	0.59
Ag	187.44	2.26	1.77	Bg	531.65	9.04	2.49
Bg	201.26	3.17	2.31	Bg	525.61	1.98	0.55
Bg	240.69	5.24	3.20	Ag	505.78	2.99	0.87
Bg	218.56	0.63	0.42	Bg	526.64	3.40	0.95
Ag	259.36	6.07	3.44	Bg	549.25	4.35	1.16
Ag	244.55	3.60	2.16	Ag	552.78	2.55	0.68
Bg	245.52	2.54	1.52	Bg	566.28	3.55	0.92
Ag	242.15	1.96	1.19	Bg	614.39	4.56	1.09
Bg	278.31	6.48	3.42	Ag	627.18	4.47	1.05
Ag	265.26	2.63	1.45	Ag	674.17	11.39	2.48
Ag	266.23	1.55	0.86	Ag	659.02	1.29	0.29
Bg	277.71	3.76	1.99	Ag	739.86	5.81	1.15
Ag	285.60	5.14	2.64	Bg	734.84	5.14	1.03
Bg	277.70	1.52	0.81	Bg	747.72	4.88	0.96
Bg	283.78	2.82	1.46	Ag	796.29	2.42	0.45
Ag	305.11	5.19	2.50	Bg	825.40	3.33	0.59
Ag	337.85	6.29	2.73	Ag	841.67	3.15	0.55
Ag	359.39	2.36	0.96	Bg	864.07	3.46	0.59
Bg	384.55	9.29	3.55	Ag	871.15	4.00	0.67
Ag	358.63	4.39	1.80	Bg	879.57	4.02	0.67
Bg	346.16	1.69	0.72	Ag	937.45	3.70	0.58
Ag	360.79	3.47	1.41	Bg	945.12	3.60	0.56

Figure Captions

Figure 1: Enthalpy as a function of pressure. The zircon structure is taken as a reference.

Figure 2: (a) Raman spectra of zircon-type NdVO_4 between 1 atm and 4.9 GPa. (b) Experimental (symbols) and theoretical (lines) pressure dependence of the Raman-mode frequencies in zircon-type NdVO_4 . The dashed lines represent Raman mode not observed in the experiments.

Figure 3: (a) Raman spectra of monazite-type NdVO_4 at pressures between 5.9 GPa and 18.1 GPa. (b) Experimental (symbols) and theoretical (lines) pressure dependence of the Raman-mode frequencies in monazite-type NdVO_4 .

Figure 4: Raman spectra of NdVO_4 at pressures between 19 GPa and 30.8 GPa.

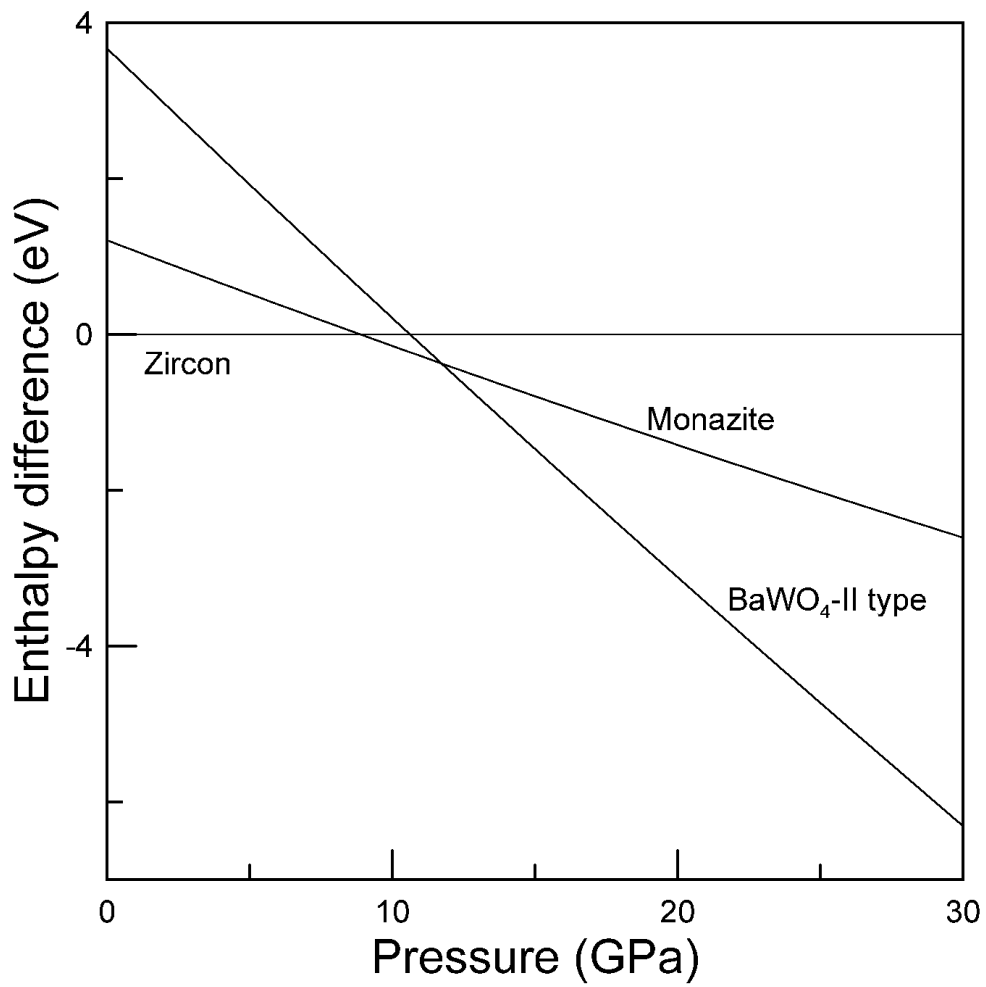


Figure 1

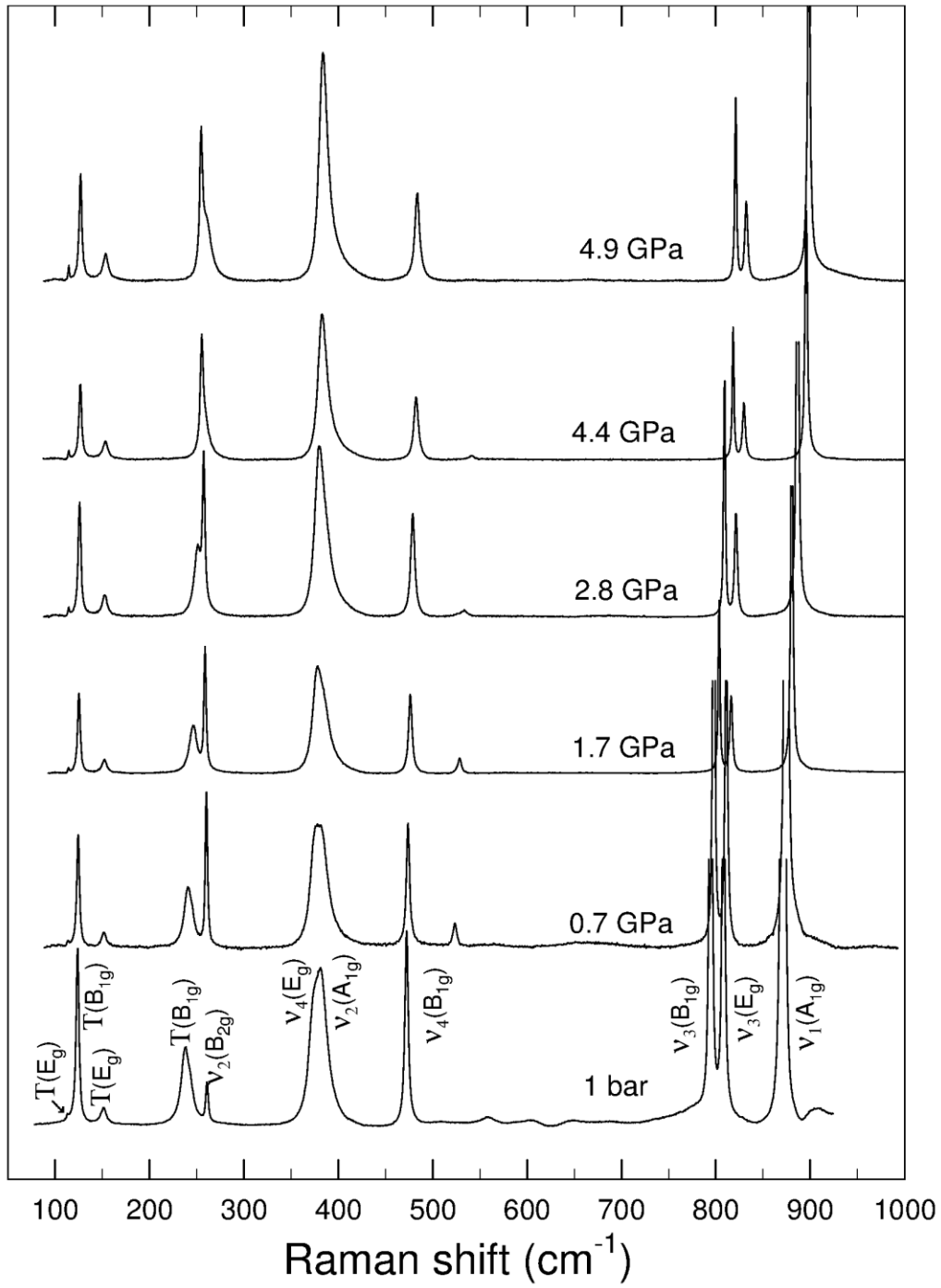


Figure 2(a)

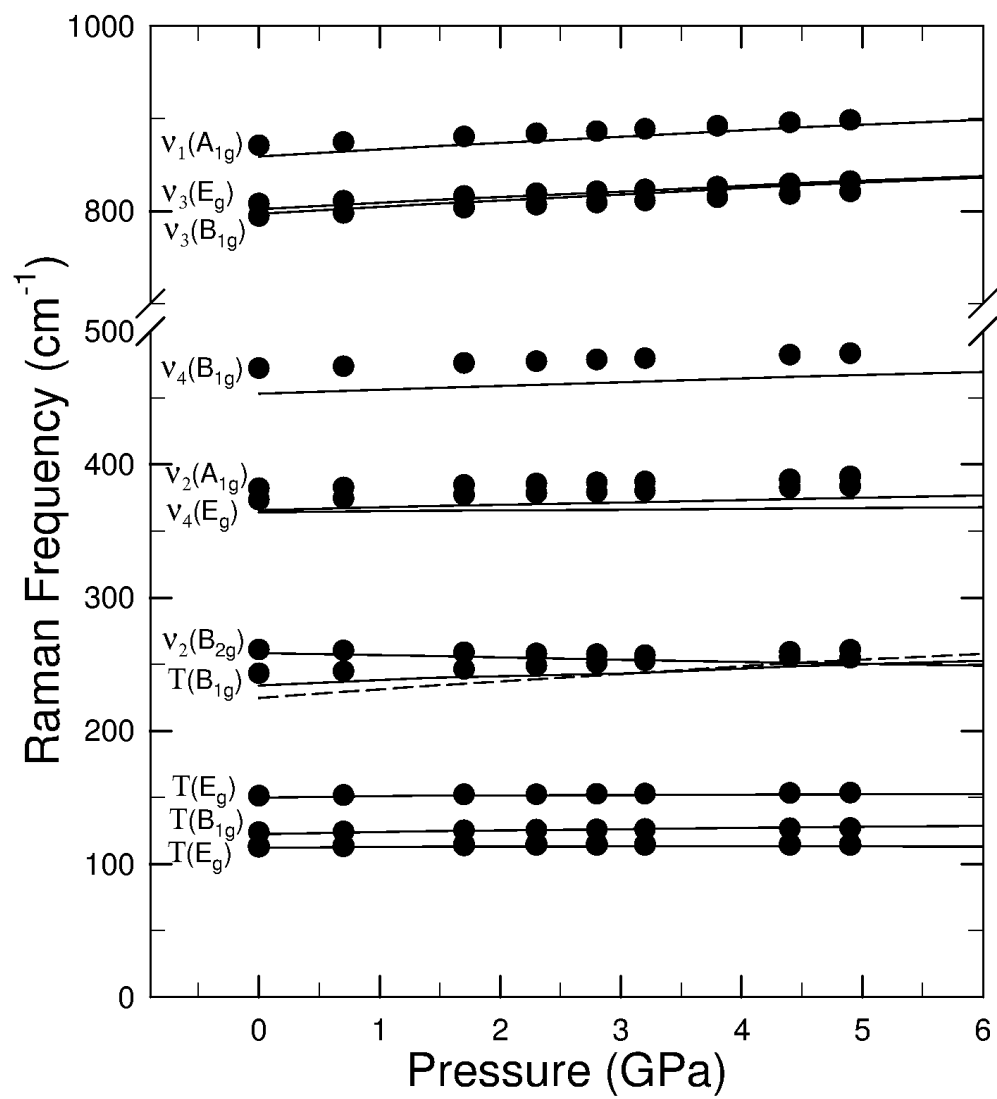


Figure 2(b)

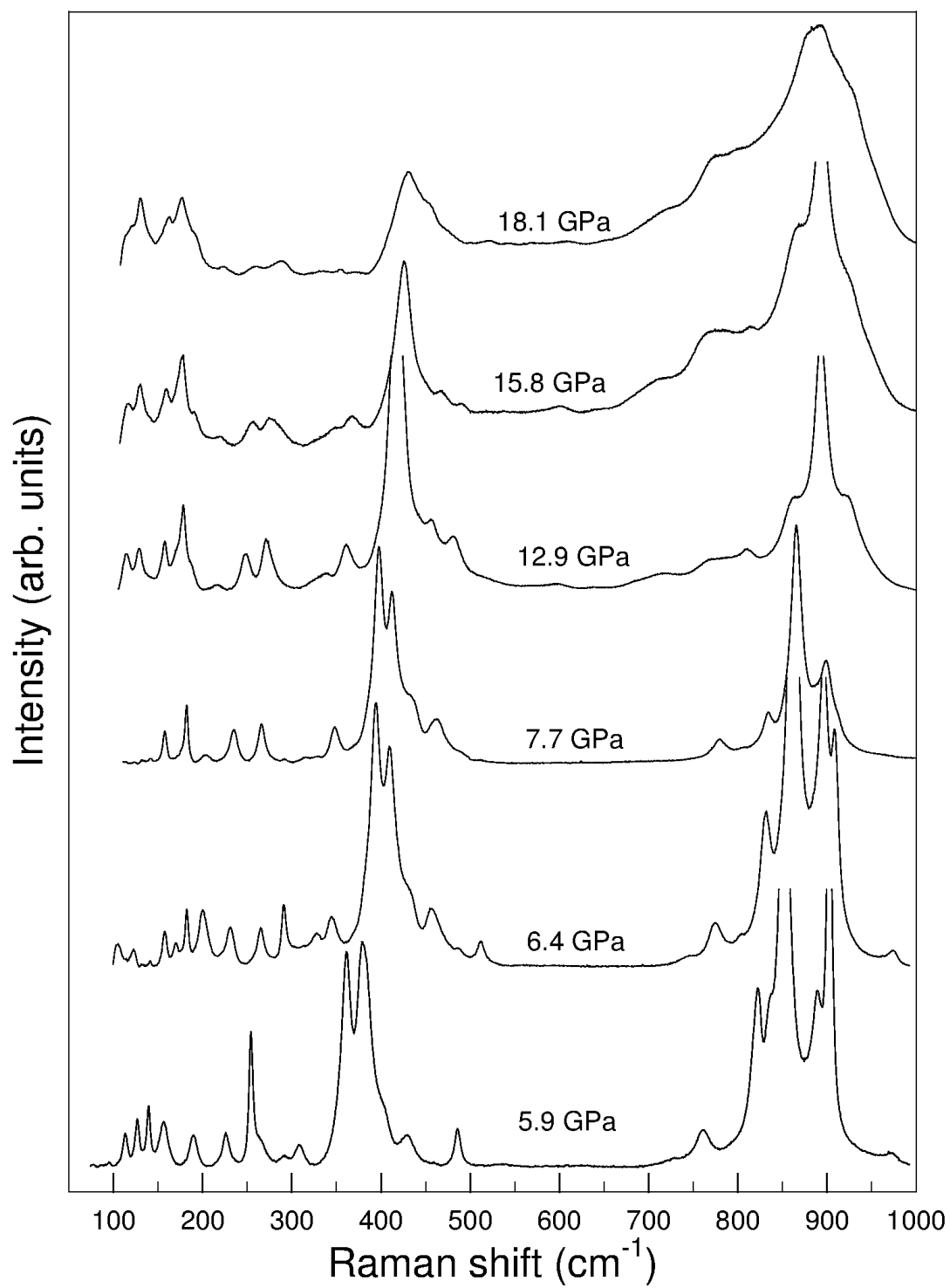


Figure 3(a)

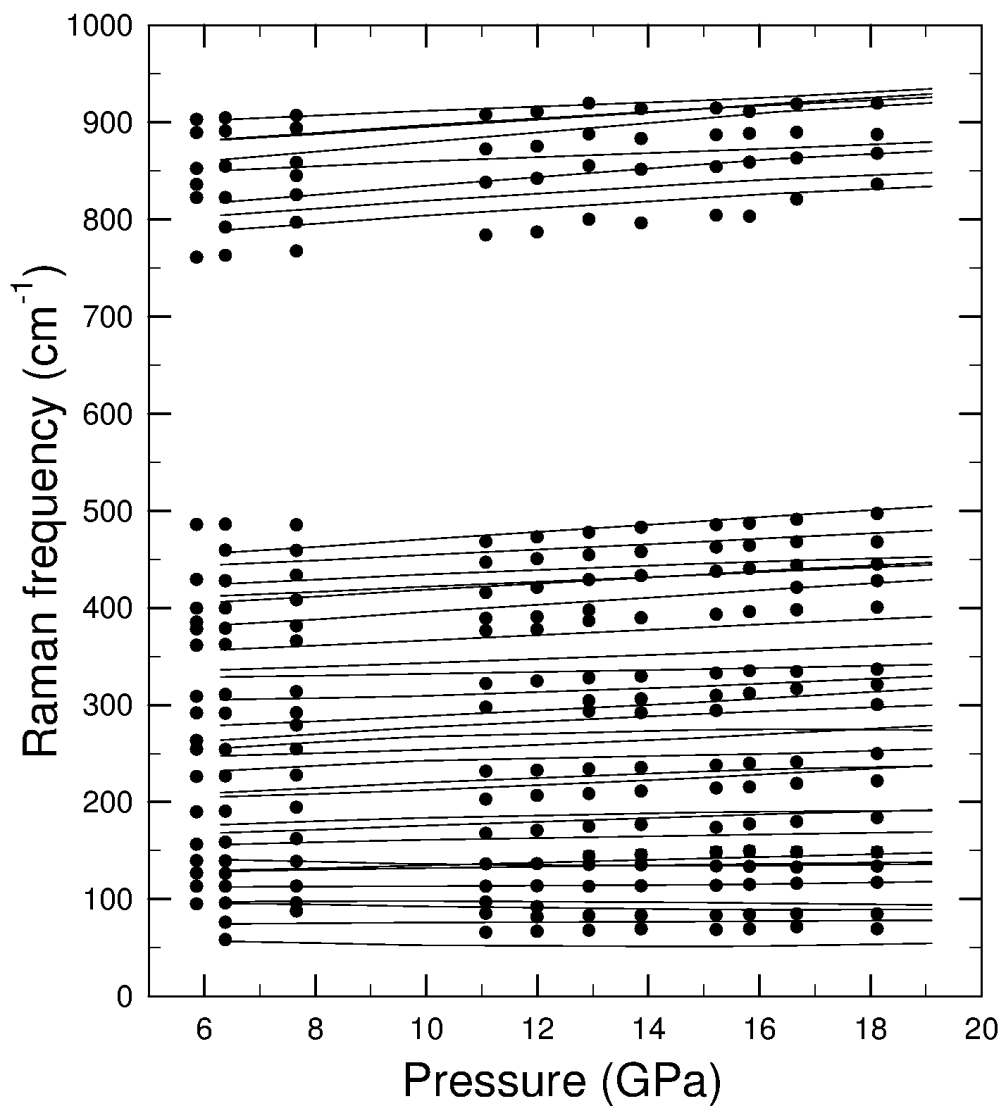


Figure 3(b)

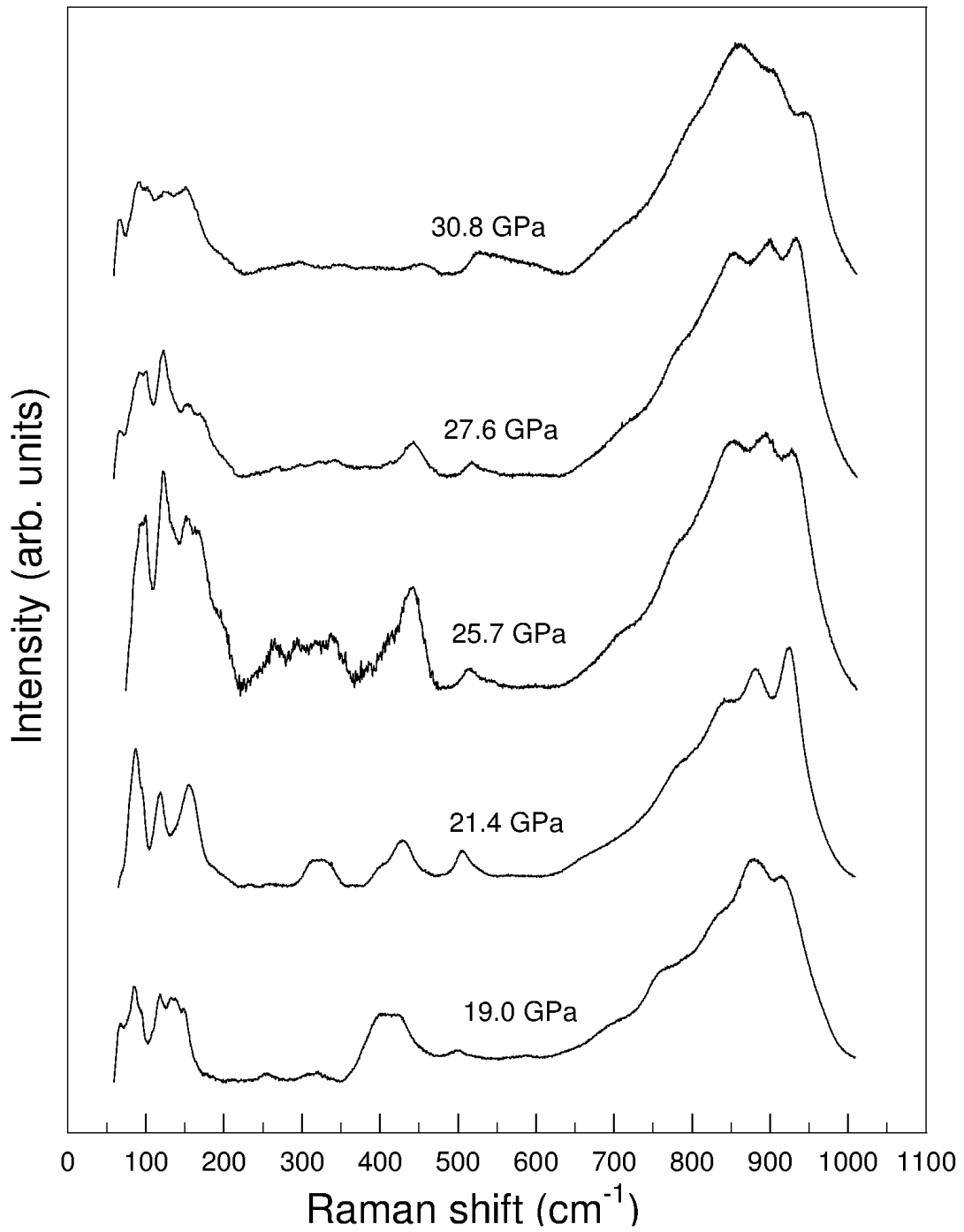


Figure 4